

# Advances in Computed Tomography Imaging Technology

Daniel Thomas Ginat<sup>1</sup> and Rajiv Gupta<sup>2</sup>

<sup>1</sup>Department of Radiology, University of Chicago, Chicago, Illinois 60637

<sup>2</sup>Department of Radiology, Massachusetts General Hospital, Boston, Massachusetts 02114; email: rgupta1@partners.org

Annu. Rev. Biomed. Eng. 2014. 16:431–53

The *Annual Review of Biomedical Engineering* is online at [bioeng.annualreviews.org](http://bioeng.annualreviews.org)

This article's doi:

[10.1146/annurev-bioeng-121813-113601](https://doi.org/10.1146/annurev-bioeng-121813-113601)

Copyright © 2014 by Annual Reviews.  
All rights reserved

## Keywords

extreme multidetector CT, iterative reconstruction, dual-energy CT, cone-beam CT, portable CT, phase-contrast CT

## Abstract

Computed tomography (CT) is an essential tool in diagnostic imaging for evaluating many clinical conditions. In recent years, there have been several notable advances in CT technology that already have had or are expected to have a significant clinical impact, including extreme multidetector CT, iterative reconstruction algorithms, dual-energy CT, cone-beam CT, portable CT, and phase-contrast CT. These techniques and their clinical applications are reviewed and illustrated in this article. In addition, emerging technologies that address deficiencies in these modalities are discussed.

## Contents

INTRODUCTION.....	432
EXTREME MULTIDETECTOR COMPUTED TOMOGRAPHY.....	435
ITERATIVE RECONSTRUCTION.....	439
DUAL-ENERGY COMPUTED TOMOGRAPHY.....	441
CONE-BEAM COMPUTED TOMOGRAPHY.....	444
PORTABLE COMPUTED TOMOGRAPHY.....	445
PHASE-CONTRAST COMPUTED TOMOGRAPHY.....	448

## INTRODUCTION

Since its inception in 1971, computed tomography (CT) has become a prolific diagnostic imaging tool, with over 70,000,000 exams performed annually in the United States (1). Indeed, there are numerous indications for performing CT-based exams, including evaluation of cerebrovascular disease, intracranial hemorrhage, sinusitis, pulmonary embolism, aortic dissection, fractures, and many tumors (2).

The speed and accuracy with which CT can be obtained to diagnose many conditions largely account for the desirability of this modality among ordering clinicians. However, there are drawbacks and limitations of CT, notably the exposure to ionizing radiation and the potential for misdiagnosis of certain diseases (3). Typical effective radiation doses in adults range from about 2 mSv (0.2 rad) for head CTs to about 8–10 mSv for CTs of the chest, abdomen, or pelvis (4). Although CT provides superior delineation of fine bony detail, magnetic resonance imaging (MRI) provides inherently better soft-tissue contrast than CT does. For example, MRI with contrast is more sensitive than CT with contrast for the detection of brain metastases from small-cell lung cancer (5).

The basic components of a standard diagnostic CT scanner include an X-ray source and a detector, positioned on opposite ends of the patient, mounted on a rotational gantry that can spin this imaging chain at very high speeds. A cross-sectional image is created by mathematical reconstruction of the measured X-ray intensities received by the detector at different positions around the patient in a circular orbit. Different tissues each have a different X-ray attenuation coefficient,  $\mu$ . The attenuation coefficients can be derived from the following equation (Beer–Lambert law) (6):

$$I = I_0 e^{-\mu x},$$

where  $I$  is the intensity of the detected X-ray,  $I_0$  is the intensity of the incident X-ray, and  $x$  is the thickness of the tissue that the X-ray beam traverses. The attenuation coefficients for different materials can be normalized with respect to the coefficient for water ( $\mu_w$ ), and the result is expressed in terms of Hounsfield units (HU) (7):

$$\text{HU} = 1000 \times \frac{\mu - \mu_w}{\mu_w}.$$

A CT image comprises a gray scale representation of the HU for each pixel, whereby each HU represents 0.1% of the attenuation of water. The HU, measured on the image by drawing regions of interest, provide insights into the nature of the tissues and lesions (**Figure 1**).

Although the fundamental physical principles of CT imaging endure, many modifications have been introduced since the first clinical CT scanner (EMI Mark I) was developed in 1971. The original EMI scanner was used only for head imaging and comprised a single, narrow beam and a

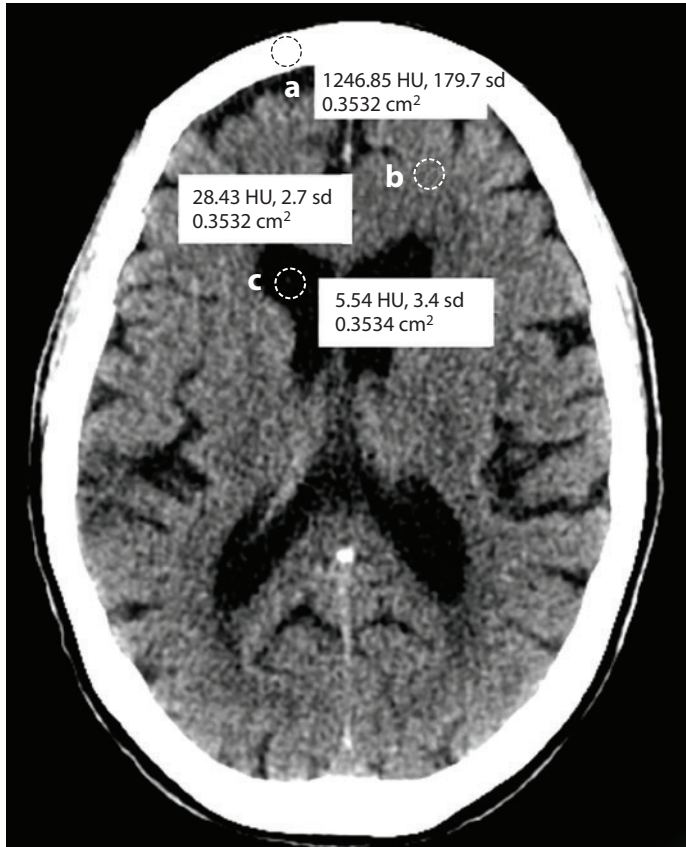


**Figure 1**

An axial computed tomography (CT) image of the head shows regions of interest (*dashed circles*) drawn over the (a) skull, (b) brain, and (c) lateral ventricle, with Hounsfield units (HU), standard deviation for the HU measurement, and area of each region of interest displayed.

single-detector assembly that operated with a rotate-translate motion (**Figure 2**) (8, 9). Acquiring 160 rays over 80° per slice, a single scan required several minutes to complete. Reduced scan times were made possible with the introduction of second-generation CT geometry consisting of multiple, narrow X-ray beams and multiple detectors. Like first-generation scanners, second-generation scanners used a rotate-translate motion. However, second-generation scanners featured gantries comprising multiple narrow beam sources and detectors that could acquire simultaneous views (**Figure 3**) (9). This approach decreased scan times to less than 20 s, thereby enabling body imaging. However, the complex mechanics of rotate-translate geometry was an obstacle for achieving even faster scan times. Third-generation CT scanners featured rotate-rotate geometry, whereby the tube and the detectors rotated together around the patient (**Figure 4**). In conjunction with a wide X-ray fan beam that encompassed the entire patient cross-section and an array of detectors to intercept the beam, scan times of less than 5 s could be achieved. However, third-generation CT scanners were prone to ring artifacts that resulted in drift in the calibration of one detector relative to the other detectors (10). Fourth-generation scanners featured stationary ring detectors and a rotating fan-beam X-ray tube (**Figure 5**), which mitigated the issues related to ring artifacts. However, the ring-detector arrangement limited the use of scatter reduction.

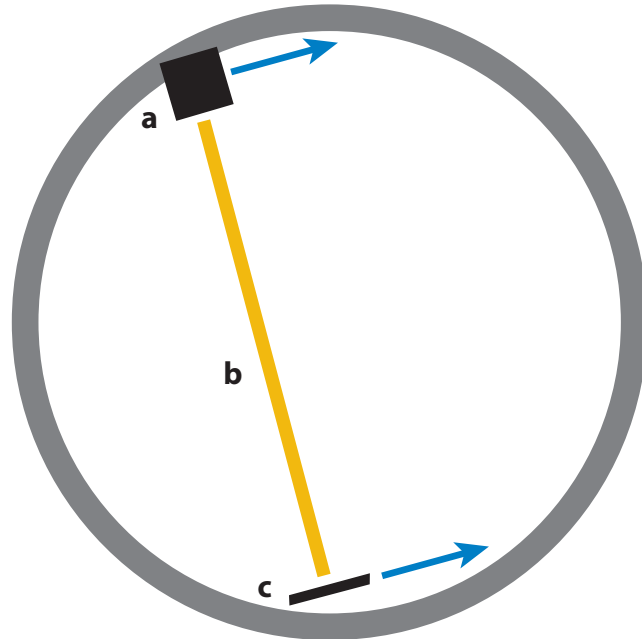


**Figure 2**

Schematic of a first-generation computed tomography (CT) scanner. The diagram shows (a) a single X-ray source that produces (b) a pencil beam incident upon (c) a single detector. The source and detector translate together at a certain angle with respect to the patient. The process is repeated at  $1^\circ$  intervals for a total of  $180^\circ$ .

The advent of slip-ring technology, which supplies continuous electrical supply to the rotating gantry without fixed connection, eliminated the time necessary for braking, and reversal of spooled cables enabled the development of the faster, helical (spiral or volume) CT, which offered greater spatial and temporal resolution (11, 12). The progression from single-detector-row to multidetector-row CT scanning further reduced scan times, with 4–64-detector-row helical CT scanners now in routine clinical use. Indeed, with multidetector helical CT, the X-ray tube continuously rotates as the patient table translates through the bore of the scanner, enabling the entire body to be scanned with submillimeter resolution during one breath hold.

Certain physical constraints must be considered in the design of faster CT scanners, notably the heating capacity of the rotating anode in the X-ray tube and the centripetal force of the rotating gantry. The buildup of heat in the anode from interaction with electrons can be significant during continuous scanning and can result in damage to the anode disc at the focal spot. The heat (J) generated in the anode focal spot is a function of  $w$  (the waveform factor), kVp (kilovolt peak), and mAs (milliampere-second):

$$\text{Heat (J)} = w \times \text{kVp} \times \text{mAs}.$$

In earlier systems, the rotating anode discs were cooled via radiation, which required idle time between exposures (13). In order to accommodate higher scan power, shorter rotation times, shorter cooling times, and smaller focal spots, convective and active cooling systems were introduced. Additionally, the X-ray tubes in rapidly rotating helical CT gantries must be able to withstand g-forces greater than 20 g without introducing vibrations and extraneous electronic noise that can undermine image quality, particularly with wider bore scanners and gantry rotation times of less

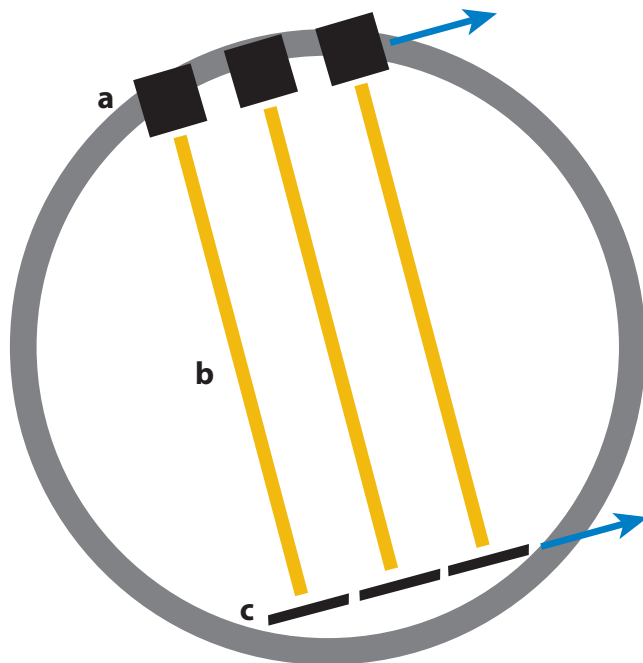


**Figure 3**

Schematic of a second-generation computed tomography (CT) scanner. The diagram shows (a) a row of multiple X-ray sources that produce (b) pencil beams incident upon (c) multiple detectors. As with first-generation scanners, the source and detector translate together at a certain angle with respect to the patient. The process is repeated at  $1^\circ$  intervals for a total of  $180^\circ$ .

than 500 ms (13). Solutions have included computer modeling, eliminating gantry tilt, and using high-precision ball-bearing components.

The increased scope of clinical applications made possible by fast multidetector helical CT scanners has resulted in increased utilization of this modality, which has in turn heightened concerns regarding radiation dose to patients. Indeed, multidetector CT imparts a higher dose profile than single-detector CT, as much as 27% higher in the plane and 69% higher in the adjacent plane of the scanned area (14). Various strategies for decreasing radiation dose, such as increasing pitch and lowering tube current, have been implemented (15). In addition, automatic tube-current modulation systems have optimized image quality and decreased radiation exposure without arbitrary selection of tube current by operators (13, 16). More recent innovations in CT technology have also resulted in better image quality, more widespread applications, and lower radiation doses. Notable advances reviewed in more detail in the following sections include extreme multidetector CT, iterative reconstruction algorithms, dual-energy CT (DECT), cone-beam CT (CBCT), portable CT, and phase-contrast CT.

## EXTREME MULTIDETECTOR COMPUTED TOMOGRAPHY

A typical multidetector CT scanner consists of a mosaic of scintillators that convert X-rays into light in the visible spectrum, a photodiode array that converts the light into an electrical signal, a switching array that enables switching between channels, and a connector that conveys the signal to a data acquisition system (**Figure 6**). The multiple channels between the detectors acquire

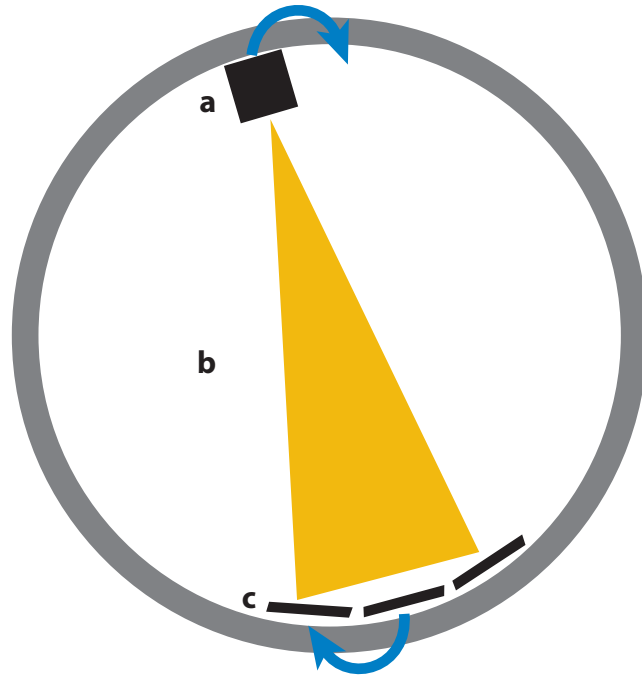


**Figure 4**

Schematic of a third-generation computed tomography (CT) scanner. The diagram shows (a) a single X-ray source that produces (b) a fan beam incident upon (c) multiple detectors. The source and detectors rotate together around the patient.

multiple sets of projection data for each rotation of the scanner gantry. The channels can sample different detector elements simultaneously and can combine the signals. The detector elements can vary in size, and hybrid detectors that comprise narrow (0.5-mm, 0.625-mm, or 0.75-mm) detectors in the center with wider (1.0-mm, 1.25-mm, or 1.5-mm) detectors flanked along the sides are commonly used (17).

Earlier generations of multidetector CT scanners comprising 4–64 channel systems achieved faster scanning speeds or higher  $z$ -axis resolution than single-slice helical CT scanners. For example, owing to its high spatial resolution, 0.5-mm thin slices, and 0.3-s gantry revolution times, 64-slice CT became the state-of-the-art technology in CT imaging shortly after its clinical introduction (18, 19). Although 64-slice CT is adequate for many clinical applications, it is insufficient to rival the anatomic detail and real-time visualization provided by conventional catheter angiography. Thus, in the hopes of attaining the 0.16-mm spatial resolution offered by typical fluoroscopy tubes, while obviating invasive catheter-based procedures for characterization of steno-occlusive vascular lesions, extreme multidetector CT, including 256- and 320-row multidetector systems, has been developed (20). Although this modality cannot yet achieve fluoroscopy resolutions, extreme multidetector CT angiography (CTA) offers excellent sensitivity and negative predictive value for functional stenoses and can potentially preclude further investigation via catheter angiography and revascularization (**Figure 7**) (21). Extreme multidetector CTA also has the potential to become the optimal technique for evaluating complications following cardiac surgery (22). With regard to imaging the carotid arteries, a 256-channel CTA protocol for carotid arteries was found to yield similar vessel contrast opacification compared with 64-channel CTA, but with fewer metallic artifacts, a modest decrease in scan time, and 10% lower radiation dose (23). Whether the

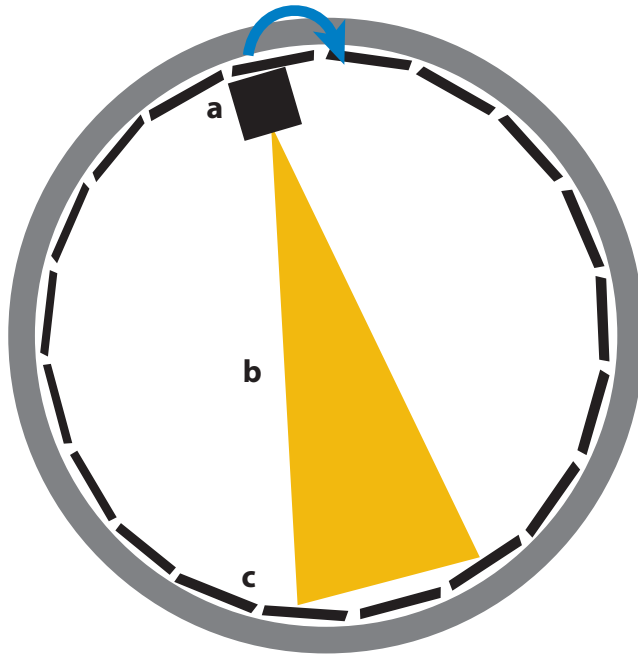


**Figure 5**

Schematic of a fourth-generation computed tomography (CT) scanner. The diagram shows (a) a single X-ray source that produces (b) a fan beam incident upon (c) a circumferential array of fixed detectors.

advantages of extreme multidetector CT ultimately yield better clinical results for management of carotid vascular disease remains to be determined. Yet another potential application of the high-spatial-resolution capabilities of extreme multidetector CT is quantitative volume imaging to determine the size of solid tumors, and monitoring tumor response during therapy should be more accurate with the smaller voxel dimensions of extreme multidetector CT and should replace the crude linear metrics typically used currently (24).

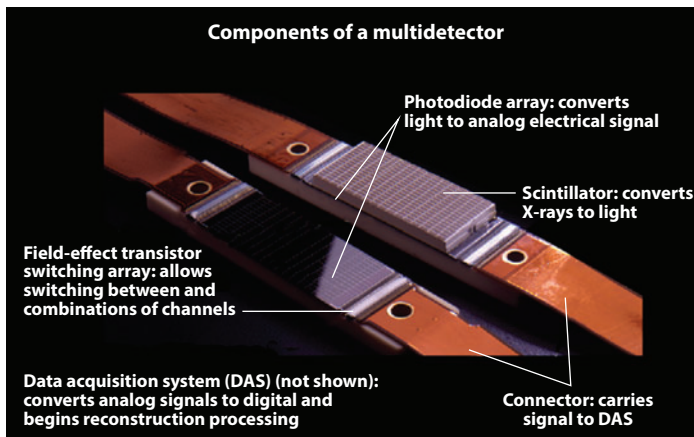


**Figure 6**

Photograph of multidetector computed tomography (CT) components.

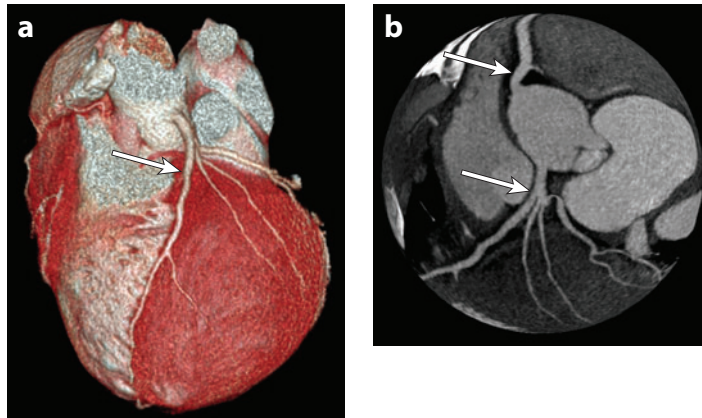


**Figure 7**

Three-dimensional (3D) extreme multidetector computed tomography (CT). (a) A surface rendering and (b) globe view from cardiac CT angiography (CTA) with a 256-row multidetector show normal coronary arteries (*arrows*).

The high temporal resolution and wide-area coverage offered by extreme multidetector CT represent a paradigm shift from an imaging modality that provides solely anatomical data to one that can also provide functional information (25). This approach is epitomized by cardiac four-dimensional (4D) electrocardiogram (ECG)-gated (cine) extreme multidetector CTA in which the heart is depicted throughout different portions of the cardiac cycle (**Figure 8**) (19). Thus, in addition to providing detailed anatomical information, cardiac CT protocols that include cine imaging sequences enable the evaluation of ejection fraction, regional wall motion abnormality, and valvular regurgitation and stenosis (26). However, it should be noted that the image quality of extreme multidetector 4D CT is inferior to that of extreme multidetector three-dimensional (3D) CT and even that of nonextreme multidetector 3D CT. Furthermore, compared with conventional angiography under fluoroscopy, which has a temporal resolution of approximately 33 ms, and echocardiography, which has a temporal resolution between 33 and 66 ms, extreme multidetector 4D CT has a higher temporal resolution of 83 ms (20). Ultimately, dynamic cardiac

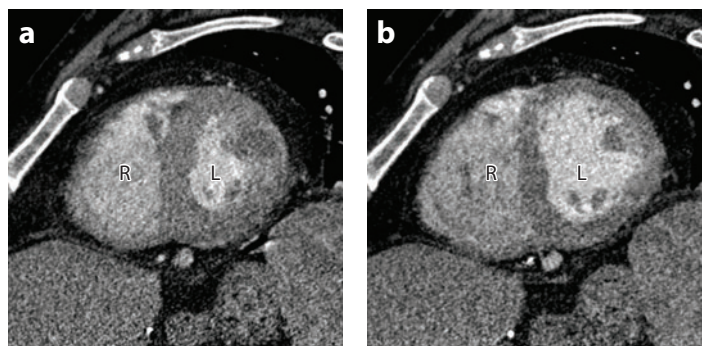


**Figure 8**

Four-dimensional (4D) extreme multidetector computed tomography (CT). Short-axis sections in (a) systole and (b) diastole from cardiac CT angiography (CTA) performed using a 256-row multidetector. The images show contraction of the right ventricle (R) and left ventricle (L), which can be used to calculate ejection fraction.

imaging via ultrasound and MRI provide clinical data essentially equivalent to those of cine extreme multidetector CT, without exposure to ionizing radiation.

A major application of 256- and 320-slice CT in neuroimaging is whole-brain 4D imaging for evaluating altered hemodynamics. Perfusion imaging performed with standard nonextreme multidetector CT does not provide whole-brain coverage and typically excludes the posterior fossa content and vertex, unless there is sufficient clinical suspicion to warrant manual adjustment of the perfusion to cover these areas at the expense of other areas of the brain. By contrast, the 16 cm of  $z$ -axis coverage possible with extreme multidetector 4D CT are sufficient to encompass the entire brain from the vertex to the craniocervical junction, thus providing potentially critical information regarding ischemic disease in vascular territories that were previously excluded (27). As a result, whole-brain perfusion with 4D multidetector CTA yields superior diagnostic accuracy compared with standard CTA, enabling the detection of additional ischemic lesions and complete coverage of otherwise partially imaged lesions (28, 29). In particular, 4D CTA can distinguish antegrade flow across a cerebral artery occlusion from retrograde collateral flow. Similarly, dynamic 4D CT can help differentiate chronic extracranial internal carotid occlusion from acute near-complete occlusion, and CT perfusion with acetazolamide challenge can provide insight into cerebrovascular reserve and the risk of future ischemia (27). However, at least with respect to patients with middle cerebral artery (MCA) territory stroke, it appears that increased levels of  $z$ -axis coverage have minimal impact upon estimating the mismatch of the infarct size on perfusion images relative to the MCA territory (30). Whole-brain perfusion imaging can potentially result in an increased frequency of incidental findings, although the impact of this increase has not yet been described in the literature.

Another potential application of dynamic scanning with extreme multidetector CT is the evaluation of joint disease, as joint motion can be directly visualized (31, 32). Thus, extreme multidetector CT systems will facilitate many important functional imaging applications that were not feasible or of adequate quality with older scanners (25). Likewise, the high spatial resolution provided by extreme multidetector CT is providing insight into various musculoskeletal conditions and more accurate diagnosis than other modalities, such as the commonly used conventional radiography. For example, one study using 320-row multidetector concluded that the radiographic appearance of juxtaarticular cyst-like lesions in the fingers may actually indicate erosions, which should lead to further clinical assessment (33).

## ITERATIVE RECONSTRUCTION

In theory, conventional filtered Fourier back-projection algorithms provide exact solutions to the inverse problem of CT image reconstruction, assuming that a complete set of noiseless transmission measurements, which represent linear functions of the attenuation line integral through the patient, is available (34). However, in actual practice, noise, scatter, beam-hardening, and high-contrast edge effects undermine this assumption, leading to data nonlinearity and artifacts such as streaking and cupping in the reconstructed image (34). As noise is inversely proportional to the square root of the radiation dose, less noisy images can be obtained by increasing the current. However, in clinical practice it is desirable to minimize radiation dose without compromising image quality.

Lange and Carson's expectation-maximization algorithm accounts for the nonlinear signal-formation processes that introduce noise in X-ray CT data and forms the basis of statistically motivated reconstruction algorithms. Although such mathematical models have actually been used in positron-emission tomography for many years, these algorithms could not be implemented in CT until recently because the computational power necessary could be achieved only with

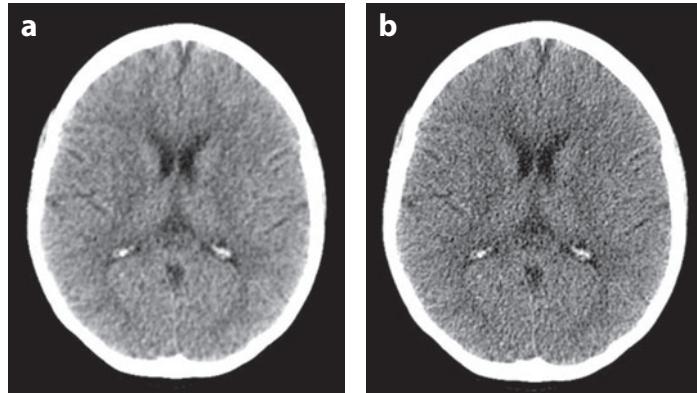


**Figure 9**

Iterative reconstruction. (a) A 90% ASiR image of the brain, which is considerably less noisy than (b) the corresponding standard filtered back-projection image.

high-performance computer processors. Several iterative reconstruction software packages are now commercially available for use in CT, including ASiR (GE Healthcare, Milwaukee, WI), IRIS (Siemens, Erlangen, Germany), Adaptive Iterative Dose Reduction (Toshiba, Tochigi, Japan), and iDose (Philips Healthcare, Best, Netherlands).

The iterative reconstruction algorithm essentially consists of a trial-and-error correction loop that is introduced in the image reconstruction process. A filtered Fourier back-projection image reconstruction is initially performed in the raw data domain in order to generate a master reconstruction. Because the filtered back projection is an approximate reconstruction, there is discordance between the measured and calculated projections. This difference is used to derive correction projections, reconstruct a correction image, and update the original image. This process is repeated until the deviation between measured and calculated projections is smaller than a predefined limit. Nonlinear image processing algorithms are used to stabilize the resolution every time the original image is updated. Thus, this regularization loop exploits prior image information with the aim of reducing image noise (35). Indeed, implementation of iterative reconstruction can yield diagnostic-quality images at 20–66% lower volume CT dose index (CTDI<sub>vol</sub>) values than those obtained with filtered Fourier back-projection techniques for head CT (**Figure 9**) as well as for CT of the chest and abdomen (36–42).

By performing a greater number of correction loops, the SAFIRE (Sinogram Affirmed Iterative REconstruction) algorithm can decrease image noise further than basic iterative reconstruction algorithms. After estimating the noise in the raw data represented by variations in adjacent voxels and subtracting this noise, SAFIRE compares the result to the initial image and generates an updated image for the next iteration (17). As a result, the image noise is decreased with each loop. Indeed, 5 and 75% radiation dose reductions can be achieved using SAFIRE for abdomen CT examinations, and image noise in sinus CT examinations can be reduced by 15–85%, depending on the iterative strength, rendering kernel, and dose parameters (17, 18). The penalty for implementing SAFIRE is an even longer reconstruction time. For example, the speed for filtered back-projection image sets is 2.9–6.6 images per second versus 0.9–1.6 images per second for SAFIRE for sinus CT (43).

Even more sophisticated iterative reconstruction techniques, such as model-based iterative reconstruction (MBIR) (Veo, GE Healthcare), can model the geometry of the CT system in addition to addressing noise. Indeed, MBIR results in 18–47% lower image noise than ASiR and, compared to Fourier back projection, enables a 78% dose reduction for abdominal CT (44, 45,

46). However, this technique requires even longer computational time than the simpler iterative reconstruction algorithms, which currently limits its clinical utility. Ultimately, this will no longer be an issue as computation power continues to improve.

## DUAL-ENERGY COMPUTED TOMOGRAPHY

Conventional CT provides a single HU for each voxel. Prior knowledge regarding the anatomy and attenuation properties of different tissues is used to distinguish various materials such as fat, bone, and muscle. However, there is often overlap of the HU of different tissues, and conventional CT is unable to distinguish materials with similar HU. For example, intracranial hemorrhage can have the same attenuation as dilute contrast or diffuse parenchymal mineralization. Different types of urinary stones (e.g., uric acid and calcium oxalate stones) are also indistinguishable from each other. Similarly, in a joint affected by gout, it is not possible to differentiate between gouty tophus and calcification, making it difficult to assess the intraarticular burden of gouty arthritis. Multispectral CT overcomes this limitation of single-energy CT by utilizing the energy dependence of HU (47). Indeed, the mass-attenuation coefficient varies based on X-ray energies for different materials. Thus, HU measured by CT are not absolute and change depending on the kVp used for image acquisition. In addition, the change in HU is material specific. This property is used by DECT for material decomposition by acquiring two image series with different kVp and assessing the change in HU to ascribe a tissue type to each voxel.

DECT can be implemented using one of the following five paradigms (47):

- Dual-spin scanners: In these scanners, two independent acquisitions, at a low- and a high-energy kV setting, are acquired sequentially. For example, one data set can be acquired at 80 kVp, and another acquired at 140 kVp. The protocol for each of these data sets can be individually optimized with filters and with tube-current modulation. There is also no cross scatter between the two sets of projections. Because these are conventional scanners, based on the traditional single-source, single-detector paradigm, they are also cost-effective. Typically, there is a time delay when switching from one kVp setting to another. Therefore, the main drawback of this technique is temporal misregistration between the high- and low-kVp scans. There is only rough voxel-by-voxel registration between the scans because of patient motion and the relatively long time between the two scans.
- Fast kVp switching: Scanners of this type employ a special X-ray tube that is capable of rapidly switching between high- and low-voltage settings on a projection-by-projection basis. This scheme requires technology for fast kV switching, a nontrivial technical task. It also requires an ultrafast detector because twice as many projections have to be acquired in each rotation. Because the individual projections in the low- and high-kVp data sets are temporally close to one another, projection-level material decomposition can be performed. The reconstructed data sets are also matched on a voxel-by-voxel basis without any misregistration. Because the low- and high-energy projections are interleaved but separated in time, scatter from one acquisition does not contaminate the other. A drawback of fast kV switching is that there is overlap between the low- and high-energy spectra, and it is not possible to selectively interpose a filter in the high-energy exposure to increase its spectral separation. The current technology also does not allow modulation of tube current while tube voltage is alternately changed between a high and a low setting. Because the dose cannot be individually optimized for the low- and high-energy data sets, there is a slightly increased radiation dose in the DECT mode.
- Dual-source scanners: As the name implies, these scanners have two independent imaging chains mounted on a single CT gantry. One imaging chain is operated in the low-energy mode, and the other imaging chain is operated in the high-energy mode. They can, therefore,

simultaneously acquire two independent data sets, one at low and another at high energy. Each imaging chain can be individually optimized, and the tube current can be modulated if necessary. It is also possible to filter the high-energy imaging chain—for example, with a tin filter—in order to maximize the spectral separation between the high- and low-energy projections. The imaging chains are typically mounted at 90° to each other. Therefore, the projections are asynchronous, and projection level decomposition is not possible. Because the two imaging chains are on simultaneously, the scatter from one can contaminate the other.

- **Dual-layer detectors:** The previous three paradigms operate the X-ray source at low and then high energy in order to accomplish dual-energy scanning. With dual-layer detectors, the X-ray source is polychromatic. It is therefore possible to acquire a low- and a high-energy spectral band from a single exposure. These scanners use a single X-ray source that is operated at one peak voltage, typically 120 or 140 kVp. The detector elements have two scintillator layers that are sensitive to two different parts of the incident X-ray spectrum. Each projection generates high- and low-energy images that are perfectly registered with each other. This allows synchronous projections, projection-level dual-energy processing, immunity from cross scatter, and tube-current modulation to optimize dose. Another major advantage of this paradigm is that fact that dual-energy processing can be performed retrospectively.
- **Photon-counting detectors:** Whereas dual-layer scanners integrate the deposited energy in two separate spectral bands, photon-counting detectors segregate incoming photons into two different bins according to the photon energy. Anywhere from two to eight bins may be used, allowing decomposition of each projection into that many spectral bands. By appropriately setting the noise threshold, an operator can nearly completely eliminate the electronic noise using these detectors. Different spectral bands can also be appropriately weighted according to their information content to improve contrast resolution, and these scanners effectively function as true multispectral CT scanners. CT scanners based on photon-counting detectors have experimentally demonstrated significant contrast improvement, noise reduction, dose reduction, and multienergy imaging. Multiple challenges, however, persist in building a stable prototype. These challenges include photon pileup, charge sharing between detector elements, detector polarization after prolonged operation, and inability to properly deal with the high peak photon flux typical of CT scanning. For these reasons, these scanners are still under development, and commercial versions are not available.

Irrespective of how different energy bands are acquired, the postprocessing steps for the five paradigms listed above are very similar. For each voxel, the total attenuation decreases with increasing X-ray photon energy, and the decrease is characteristic of the material composition of each voxel. At the energies used in medical imaging, the voxel attenuation is dependent on two main phenomena: photoelectric effect and Compton scattering. Photoelectric effect is the dominant process at low photon energies, is large for high-atomic-number (high- $Z$ ) materials such as iodine, and is approximately proportional to the third power of  $Z$ . Compton scattering, by contrast, dominates at the higher photon energies and is dependent on both the physical and electron density of the material.

Material-density images are created from DECT based on the theory of basis material decomposition (**Figure 10**). The attenuation coefficients of any material can be calculated as a weighted sum of the attenuation coefficients of two basis materials (e.g., iodine and water), as long as the  $k$ -edge of the material is not within the evaluated energy range (48). This works best if the two materials have sufficiently different  $Z$ s.

DECT can be used for material characterization (e.g., for differentiating hemorrhage from iodine or calcification), plaque characterization, automatic bone removal, stone characterization, and assessment of gout. It can also be used as a quantitative tool—for example, for assessing the

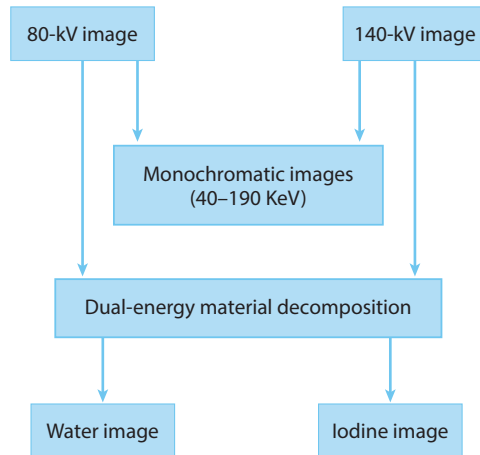


**Figure 10**

Postprocessing steps in dual-energy computed tomography (DECT). The schematic shows the typical postprocessing steps used when analyzing DECT data sets. The low- and high-energy images, in either the projection or reconstructed domain, can be decomposed into canonical pairs of two materials—for example, water and iodine—in contrast-enhanced DECT. In this decomposition, the water image represents materials that have spectral signatures close to that of water, and the iodine image represents materials that have signatures close to that of iodine.

degree of enhancement of a tumor in oncologic applications and for CT perfusion. Most DECT postprocessing packages also allow generation of virtual monochromatic images that may be used for optimal contrast viewing, posterior fossa artifact reduction, and metal artifact reduction. In the literature, the following clinical applications of DECT have been described (49–55):

- Differentiation of hemorrhage from iodinated-contrast staining that can occur after endovascular thrombectomy in patients with cerebral ischemia (**Figure 11**)

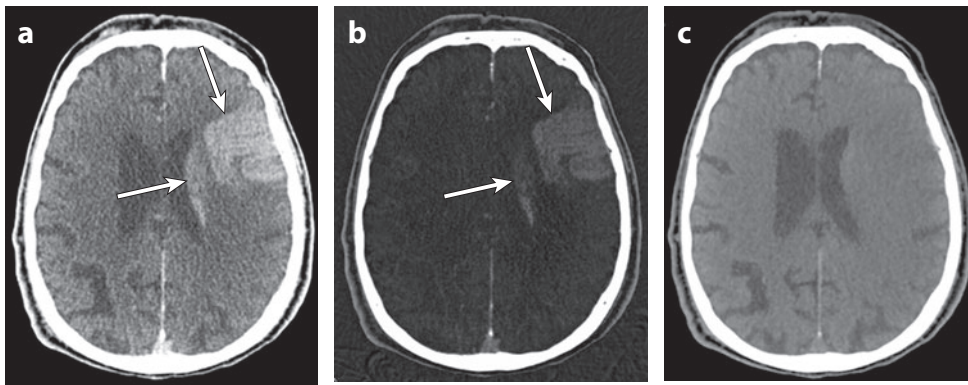


**Figure 11**

Dual-energy computed tomography (DECT). The patient had an acute left middle cerebral artery territory infarct and underwent recent cerebral angiography. This study was obtained to differentiate contrast from hemorrhage. (a) An axial SE-120-kV CT image and (b) corresponding iodine overlay image show hyperattenuation within the left frontal lobe and caudate nucleus (arrows). The absence of hyperattenuation on (c) the virtual noncontrast image confirms the presence of contrast staining rather than hemorrhage. Abbreviation: CT, computed tomography; SE, single energy.

- Calcified plaque and bone subtraction for CTA in order to discern the contrast-opacified vessels from adjacent bone, particularly in the skull base and vertebrae
- Evaluation of extracranial-intracranial bypass surgery
- Lung nodule characterization
- Myocardial iron detection
- Gallstone characterization
- Renal stone characterization and detection on contrast-enhanced images
- Renal cyst and mass characterization
- Differentiating gout from pseudogout
- Metal artifact reduction

Limitations of DECT include a relatively small field of view (FOV) (with dual-source CT), a slight increase in radiation dose, and noisy low-energy (80 kVp) images (49). Studies of dual-source CT with a 26-cm FOV revealed a higher radiation dose in comparison with single-energy acquisitions (49). Adding a tin filter in front of the higher-kV source improves spectral separation and may decrease the radiation dose. Beam-hardening artifacts can be observed in thorax perfusion DECT owing to the dense contrast in the superior vena cava, which can mimic an embolus. These artifacts can be minimized by the use of a saline flush and caudocranial scanning.

## CONE-BEAM COMPUTED TOMOGRAPHY

Unlike the X-ray fan-beam geometry of conventional CT scanners, CBCT systems produce an X-ray beam in a conical configuration that enables a volume of tissue to be imaged in a single rotation (**Figure 12, left**). The cone angle of the X-ray beam can be increased by increasing the

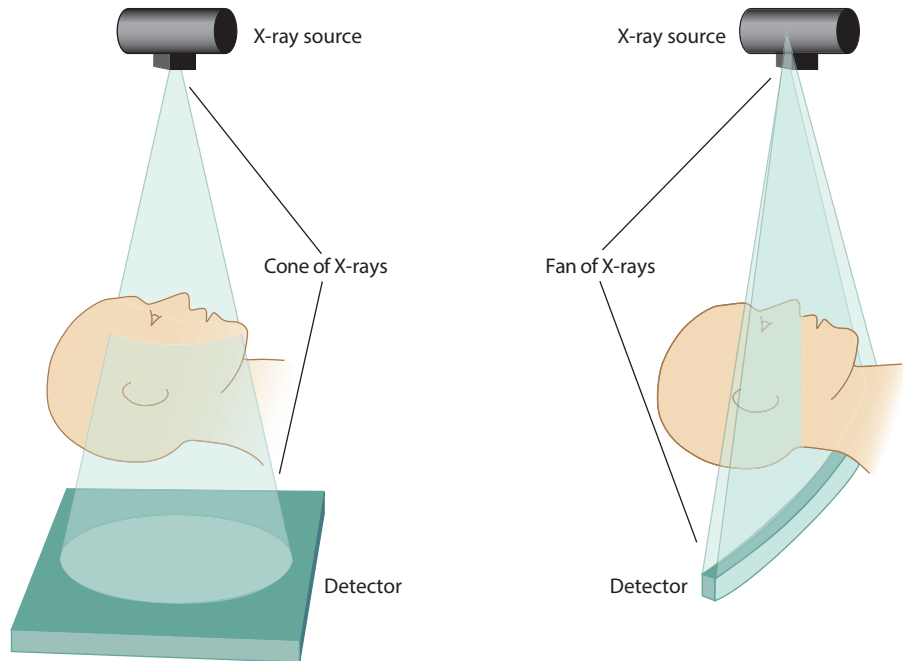


**Figure 12**

Schematic of the X-ray source configuration in (*left*) cone-beam computed tomography versus (*right*) fan-beam computed tomography.

anode angle in the X-ray tube. A rectangular or round two-dimensional (2D) detector captures the projection data of the entire region of interest in a single rotation. The reconstruction algorithm most frequently used in CBCT is a modified Feldkamp algorithm, which is essentially a 3D adaptation of the filtered back-projection method used in fan-beam 2D reconstructions (56).

The development of CBCT scanners has been enabled by several technological advances, including the development of compact, relatively low-cost, high-quality, large-area, flat-panel detector arrays; the availability of low-cost computers with processing power sufficient for cone-beam image reconstruction in near real time; and the fabrication of highly efficient X-ray tubes capable of multiple exposures necessary for cone-beam scanning (and at prices lower than those to fabricate the tubes used for fan-beam CT).

A flat-panel detector converts X-ray energy into electrical signals for digitization. It consists of a film of scintillator crystals that overlie a matrix of photodiodes formed in a solid-state amorphous silicone substrate (56). The 2D FOV observed by a flat-panel detector can be refreshed at the video frame rate, which governs the rate at which projection data are acquired as the gantry is rotated. The imaging chain of a flat-panel-based CBCT scanner can be mounted on multiple different types of mechanical gantries for rotation. These include specialized gantries for dental and maxillofacial imagers; a C-arm, conventional CT gantry; and radiation therapy systems in which CBCT provides an auxiliary imaging chain for precise registration and alignment. CBCT is typically implemented as a seat scanner such that the imaging chain is rotated around a vertical axis with the patient seated at the isocenter (**Figure 13**). These systems are compact and suitable for use in an office setting.

The main advantages of flat-panel-based CBCT include high (150- $\mu\text{m}$ ) spatial resolution, high-volume coverage, ability to perform fluoroscopy/angiography in conjunction with tomography, and ability to monitor a temporally evolving process. For example, imaging of the paranasal sinuses is possible with delivery of approximately 0.2 mSv (57). These advantages are counterbalanced by lower contrast resolution, slower decay time of scintillation material, and longer scan time (i.e., on the order of 3 to 20 s) (58). The main factors that are responsible for the limited contrast resolution of CBCT include increased X-ray scatter in cone-beam acquisition and lower detective quantum efficiency compared with multidetector CT (56).

The high resolution of flat-panel CBCT is advantageous for many clinical applications in dental imaging, temporal bone imaging, sinonasal imaging, musculoskeletal imaging, breast imaging, and imaging of implanted devices (e.g., prostheses, endovascular coils, and stents) (**Figure 14**) (59–64). Other potential applications for flat-panel CBCT include small-animal imaging, tissue-engineering experiments, and intraoperative imaging (65, 66). Improvements in scatter subtraction methods continue to be the subject of research aimed at improving image quality in CBCT systems. Several approaches have been studied, including Monte Carlo simulations, blocker-based or beam-stop techniques, analytic calculations, and collimator shadow estimation (67, 68).

## PORTABLE COMPUTED TOMOGRAPHY

Standard CT scanners are stationary and require patients to travel to a dedicated CT suite, where there is a high-voltage power source, wall and ceiling shielding, and a technologist control room. These scanners are inaccessible to certain patient populations, such as critically ill patients in intensive care units (ICUs) as well as patients undergoing surgery. For example, transporting critically ill patients outside of ICUs has been associated with a 71% incidence of adverse events occurring during the transport to CT scanners (69). Likewise, there is often a need for perioperative cross-sectional image guidance in order to improve surgical precision and minimize the risk of complications, particularly for the implantation of various devices, fracture reduction, and tumor



**Figure 13**

Photograph of a clinical cone-beam computed tomography scanner (Accuitomo, J. Morita MFG Corp., Kyoto, Japan).

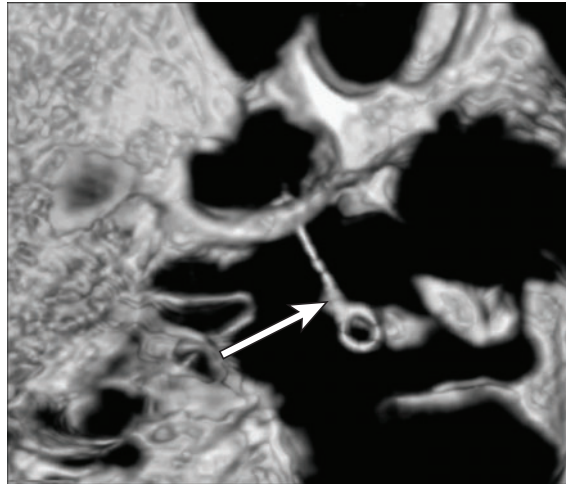


**Figure 14**

Cone-beam computed tomography of the temporal bone. The three-dimensional image shows high-resolution detail of the wire loop ossicular prosthesis (*arrow*).



**Figure 15**

Photograph of a portable computed tomography scanner (CereTom, NeuroLogica Corporation, Danvers, MA).

resection, in which direct or endoscopic visualization may be insufficient. Portable (mobile) CT scanners have been developed to address these issues.

Several portable CT scanners are now commercially available, including CereTom (**Figure 15**), Tomoscan (Philips Medical Systems), xCAT ENT (Xoran Technologies, Ann Arbor, MI), BodyTom (NeuroLogica, Danvers, MA), and OTOScan (NeuroLogica) (70). Tomoscan comprises a gantry with multisection detectors and detachable table. OTOScan is a multidetector CT that is used mainly for imaging the ear, the nose, and the throat. xCAT ENT is a CBCT that is used mainly for intraoperative scanning of the skull and sinuses. The high resolution provided by CBCT is particularly useful for perioperative evaluation during dental, spine, sinus, and temporal bone surgery. Indeed, one study (71) showed that intraoperative scanning with this modality altered the surgical plan in 30% of sinonasal cases. Although intraoperative MRI can provide superb detail of brain tumors (72), portable CT scanners offer the advantage of faster scan times.

Several key technical considerations are involved in creating an effective portable CT unit. For example, the CereTom scanner includes the following features (73):

- Casters for transporting the approximately 750-lb scanner to the patient and a centipede track system for scanning the patient at 1.25-mm, 2.5-mm, or 10-mm sections
- Battery power, which can be recharged using a 120-V source (As the X-ray tube is relatively close to the patient, less power is needed to achieve diagnostic image quality.)
- Monoblock technology, in which the X-ray tube and the high-voltage generator are incorporated into a single casing, reducing the size of the X-ray tube
- Eight rows of 1.25-mm-wide efficient solid-state detectors to compensate for low tube currents
- A command tower with a laptop computer that can enable immediate image interpretation

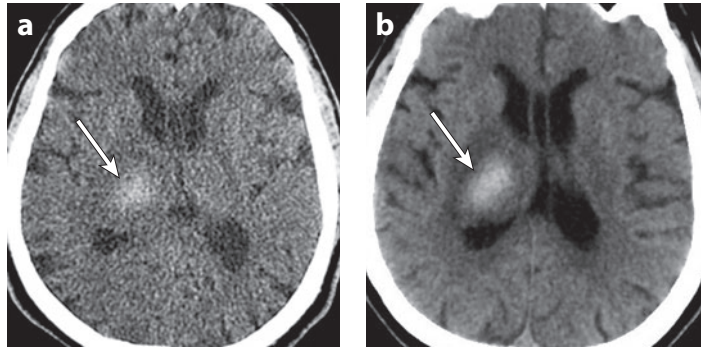


**Figure 16**

Portable computed tomography (CT). Axial CT images acquired using (a) a portable scanner and (b) a conventional scanner and obtained within several hours of one another show a right thalamus hematoma with surrounding vasogenic edema (*arrows*). The abnormality is less conspicuous on the image from the portable scanner than on the image from the standard scanner, but it is still visible.

- DICOM images that can be uploaded to a PACS (picture archiving and communication system) shortly after scanning

The quality of portable CT images is inferior to that of images from standard clinical CT scanners. For example, the appearance of standard CT images was preferred in 98% of cases for imaging at the level of the centrum semiovale and the middle cerebellar peduncles and 93% of cases for imaging at the level of the basal ganglia (70) (**Figure 16**). Nevertheless, portable CT images are considered to be of adequate diagnostic quality, and the modality subjects the patient to a radiation dose similar to that in standard CT (70). In general, portable head CT can be reliably and cost-effectively performed in ICUs and operating rooms (74–76). The development of carbon nanotubes that can produce X-rays at room temperature with a relatively low power requirement may enable the design of portable and flexible CT scanners composed of an array of miniature X-ray emitters and detectors that could be used to image the cervical spine even before moving trauma patients (77).

## PHASE-CONTRAST COMPUTED TOMOGRAPHY

Conventional X-ray imaging is sensitive to attenuation differences arising primarily from photoelectric effect and Compton scattering. Contrast arising from these effects cannot be used to differentiate the various types of soft tissues. Furthermore, conventional X-ray imaging does not account for ultrasmall angle refraction and other processes that alter the phase of the X-ray beam based on differences in the refractive index of various tissues along the X-ray propagation path. As a result, all current X-ray modalities, including fluoroscopy, angiography, mammography, and CT, are sensitive to  $Z$  difference but not to differences in electron density.

Like that of any material, the complex refractive index of tissue ( $n$ ) can be expressed as  $n = 1 - \delta - i\beta$ , where the real term  $\delta$  is responsible for phase alterations, and the imaginary term  $\beta$  for attenuation. Imaging based on the phase-contrast term  $\delta$  produces much greater contrast in the case of biological soft tissues, which are composed primarily of low  $Z$  elements, than does imaging based on the absorption term  $\beta$ .

A variety of imaging methods have been proposed to image phase (78, 79). These include synchrotron-based methods and methods that use a traditional X-ray tube. A synchrotron provides a powerful, coherent source of X-rays with high brilliance. Using such a source, several

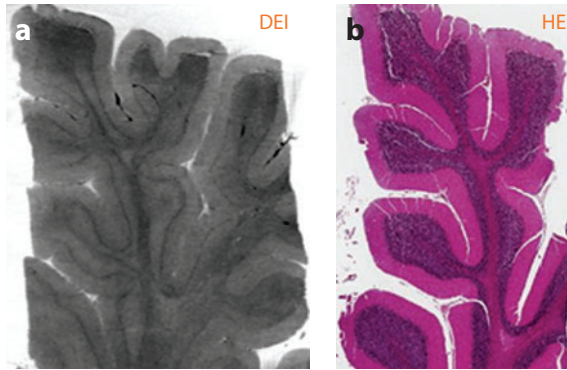


**Figure 17**

(a) Diffraction-enhanced imaging (DEI) computed tomography image of a brain specimen with (b) approximately matched hematoxylin and eosin (HE)-stained slide. (Figure courtesy of Y. Wu, M. Ando, N. Sunaguchi, T. Yuasu, and K. Hyodo, Photon Factory, KEK, Tsukuba, Japan.)

interferometry-, diffractometry-, or analyzer-based techniques have been demonstrated for phase-contrast imaging. Currently, diffraction-enhanced imaging (DEI) by means of a Bragg-case analyzer that detects the angular deviation of the incident beam due to refraction in tissues is the most widely used method in biomedical applications. DEI-CT has developed into an excellent method to delineate biological soft tissues (**Figure 17**), with further potential for use in other biomedical science applications (80).

Phase-contrast X-ray imaging can also be performed using traditional X-ray sources. The most commonly used configuration employs a sequence of gratings to implement a Talbot interferometer. A preclinical phase-contrast CT system similar to those using a synchrotron source was recently reported by Tapfer et al. (81). This system showed that X-ray CT using phase contrast can produce images with soft-tissue contrast superior to that in images from conventional attenuation-based CT. In addition, phase-contrast imaging offers very high spatial resolution down to the submicrometer level (82). Although the preclinical feasibility of phase-contrast imaging has been demonstrated, with both synchrotron-based and laboratory X-ray sources, there is currently no phase-contrast CT system available for clinical use.

As with any new modality, an inherent challenge for the introduction of phase-contrast CT into clinical use will be establishing a practical knowledge base for accurate image interpretation of both normal and pathological conditions. Color-fused image representation of the complementary absorption and phase-contrast information in a single image may facilitate this process (83). Besides this, the main technical challenges include maintaining adequate mechanical stability and spatial coherence of X-ray beams, particularly with in-line techniques (82). Instead, the use of a microfocus X-ray source based on the liquid-metal-jet anode electron impact technique can deliver an X-ray flux more than 100 times greater than that of conventional rotating anodes (84).

Ultimately, phase-contrast CT may revolutionize diagnostic radiology. Potential applications include high-contrast mammography, in which microstructures of soft biological tissues are visualized under low radiation dose; lung disease imaging, in which X-ray phase contrast can be created at the air-tissue interfaces; and musculoskeletal imaging, in which early articular cartilage defects can be discerned via a combination of high spatial resolution and detection of X-ray refraction, extinction, and absorption patterns in the DEI images; among many other possibilities (82).

Biomedical engineering has served a crucial role in advancing CT as a diagnostic imaging modality. Salient examples include extreme multidetector CT, iterative reconstruction algorithms, dual-energy CT, cone-beam CT, portable CT, and phase-contrast CT.

## DISCLOSURE STATEMENT

The authors are not aware of any affiliations, memberships, funding, or financial holdings that might be perceived as affecting the objectivity of this review.

## LITERATURE CITED

1. Am. Coll. Radiol. 2013. ACR Appropriateness Criteria<sup>®</sup>. Guidelines, Reston, VA, updated Nov. 2013, accessed Nov. 10, 2013. <http://www.acr.org/Quality-Safety/Appropriateness-Criteria>
2. Berrington de González A, Mahesh M, Kim KP, Bhargavan M, Lewis R, et al. 2009. Projected cancer risks from computed tomographic scans performed in the United States in 2007. *Arch. Intern. Med.* 169:2071–77
3. Fred HL. 2004. Drawbacks and limitations of computed tomography: views from a medical educator. *Tex. Heart Inst. J.* 31(4):345–48
4. Wiest PW, Locken JA, Heintz PH, Mettler FA Jr. 2002. CT scanning: a major source of radiation exposure. *Semin. Ultrasound CT MR* 23(5):402–10
5. Seute T, Leffers P, ten Velde GP, Twijnstra A. 2008. Detection of brain metastases from small cell lung cancer: consequences of changing imaging techniques (CT versus MRI). *Cancer* 112(8):1827–34
6. Mathieu KB, Kappadath SC, White RA, Atkinson EN, Cody DD. 2011. An empirical model of diagnostic X-ray attenuation under narrow-beam geometry. *Med. Phys.* 38(8):4546–55
7. Brooks RA, Di Chiro G. 1976. Principles of computer assisted tomography (CAT) in radiographic and radioisotopic imaging. *Phys. Med. Biol.* 21:689–732
8. Baker HL Jr, Campbell JK, Houser OW, Reese DF. 1975. Early experience with the EMI scanner for study of the brain. *Radiology* 116(02):327–33
9. Beckmann EC. 2006. CT scanning the early days. *Br. J. Radiol.* 79(937):5–8
10. Barrett JF, Keat N. 2004. Artifacts in CT: recognition and avoidance. *Radiographics* 24(6):1679–91
11. Villafana T. 1991. Technologic advances in computed tomography. *Curr. Opin. Radiol.* 3(2):275–83
12. Rigauts H, Marchal G, Baert AL, Hupke R. 1990. Initial experience with volume CT scanning. *J. Comput. Assist. Tomogr.* 14(4):675–82
13. Schardt P, Deuringer J, Freudenberger J, Hell E, Knüpfer W, et al. 2004. New X-ray tube performance in computed tomography by introducing the rotating envelope tube technology. *Med. Phys.* 31(9):2699–706
14. Thomson FJ, Paulson EK, Yoshizumi TT, Frush DP, Nelson RC. 2003. Single versus multi-detector row CT: comparison of radiation doses and dose profiles. *Acad. Radiol.* 10(4):379–85
15. Kalra MK, Maher MM, Toth TL, Hamberg LM, Blake MA, et al. 2004. Strategies for CT radiation dose optimization. *Radiology* 230:619–28
16. Kalra MK, Maher MM, Toth TL, Schmidt B, Westerman BL, et al. 2004. Techniques and applications of automatic tube current modulation for CT. *Radiology* 233:649–57
17. Saini S. 2004. Multi-detector row CT: principles and practice for abdominal applications. *Radiology* 233(2):323–27
18. Rogalla P, Kloeters C, Hein PA. 2009. CT technology overview: 64-slice and beyond. *Radiol. Clin. North Am.* 47(1):1–11
19. Hurlock GS, Higashino H, Mochizuki T. 2009. History of cardiac computed tomography: single to 320-detector row multislice computed tomography. *Int. J. Cardiovasc. Imaging* 25(Suppl. 1):31–42
20. Otero HJ, Steigner ML, Rybicki FJ. 2009. The “post-64” era of coronary CT angiography: understanding new technology from physical principles. *Radiol. Clin. North Am.* 47(1):79–90
21. Ko BS, Wong DT, Cameron JD, Leong DP, Leung M, et al. 2014. 320-row CT coronary angiography predicts freedom from revascularisation and acts as a gatekeeper to defer invasive angiography in stable coronary artery disease: a fractional flow reserve-correlated study. *Eur. Radiol.* 24:738–47
22. Bhatnagar G, Vardhanabhuti V, Nensey RR, Sidhu HS, Morgan-Hughes G, Roobottom CA. 2013. The role of multidetector computed tomography coronary angiography in imaging complications post-cardiac surgery. *Clin. Radiol.* 68(5):e254–65
23. Johnson JM, Reed MS, Burbank HN, Filippi CG. 2013. Quality of extracranial carotid evaluation with 256-section CT. *AJNR Am. J. Neuroradiol.* 34:1626–31

24. Levin DC, Rao VM, Parker L, Frangos AJ, Sunshine JH. 2005. Recent trends in utilization of cardiovascular imaging: How important are they for radiology? *J. Am. Coll. Radiol.* 2:736–39
25. Boone JM. 2006. Multidetector CT: opportunities, challenges, and concerns associated with scanners with 64 or more detector rows. *Radiology* 241:334–37
26. Nasis A, Mottram PM, Cameron JD, Seneviratne SK. 2013. Current and evolving clinical applications of multidetector cardiac CT in assessment of structural heart disease. *Radiology* 267(1):11–25
27. Snyder KV, Mokin M, Bates VE. 2014. Neurologic applications of whole-brain volumetric multidetector computed tomography. *Neurol. Clin.* 32(1):237–51
28. Frölich AM, Psychogios MN, Klotz E, Schramm R, Knauth M, Schramm P. 2012. Antegrade flow across incomplete vessel occlusions can be distinguished from retrograde collateral flow using 4-dimensional computed tomographic angiography. *Stroke* 43(11):2974–79
29. Dorn F, Muenzel D, Meier R, Poppert H, Rummeny EJ, Huber A. 2011. Brain perfusion CT for acute stroke using a 256-slice CT: improvement of diagnostic information by large volume coverage. *Eur. Radiol.* 21:1803–10
30. Furtado AD, Lau BC, Vittinghoff E, Dillon WP, Smith WS, et al. 2010. Optimal brain perfusion CT coverage in patients with acute middle cerebral artery stroke. *AJNR Am. J. Neuroradiol.* 31(4):691–95
31. Goh YP, Lau KK. 2012. Using the 320-multidetector computed tomography scanner for four-dimensional functional assessment of the elbow joint. *Am. J. Orthop. (Belle Mead, Nj)* 41(2):E20–24
32. Kalia V, Obray RW, Filice R, Fayad LM, Murphy K, Carrino JA. 2009. Functional joint imaging using 256-MDCT: technical feasibility. *Am. J. Roentgenol.* 192(6):W295–99
33. de Bucourt M, Scheurig-Münkler C, Feist E, Juran R, Diekhoff T, et al. 2012. Cyst-like lesions in finger joints detected by conventional radiography: comparison with 320-row multidetector computed tomography. *Arthritis Rheum.* 64(4):1283–90
34. Evans JD, Politte DG, Whiting BR, O’Sullivan JA, Williamson JF. 2011. Noise-resolution tradeoffs in X-ray CT imaging: a comparison of penalized alternating minimization and filtered backprojection algorithms. *Med. Phys.* 38(3):1444–58
35. Renker M, Nance JW Jr, Schoepf UJ, O’Brien TX, Zwerner PL, et al. 2011. Evaluation of heavily calcified vessels with coronary CT angiography: comparison of iterative and filtered back projection image reconstruction. *Radiology* 260:390–99
36. Rapalino O, Kamalian S, Kamalian S, Payabvash S, Souza LC, et al. 2012. Cranial CT with adaptive statistical iterative reconstruction: improved image quality with concomitant radiation dose reduction. *AJNR Am. J. Neuroradiol.* 33:609–15
37. Korn A, Fenchel M, Bender B, Danz S, Hauser TK, et al. 2012. Iterative reconstruction in head CT: image quality of routine and low-dose protocols in comparison with standard filtered back-projection. *AJNR Am. J. Neuroradiol.* 33:218–24
38. Vorona GA, Zuccoli G, Sutcavage T, Clayton BL, Ceschin RC, Panigrahy A. 2013. The use of adaptive statistical iterative reconstruction in pediatric head CT: a feasibility study. *AJNR Am. J. Neuroradiol.* 34:205–11
39. Hara AK, Paden RG, Silva AC, Kujak JL, Lawder HJ, Pavlicek W. 2009. Iterative reconstruction technique for reducing body radiation dose at CT: feasibility study. *Am. J. Roentgenol.* 193:764–71
40. Prakash P, Kalra MK, Kambadakone AK, Pien H, Hsieh J, et al. 2010. Reducing abdominal CT radiation dose with adaptive statistical iterative reconstruction technique. *Investig. Radiol.* 45:202–10
41. Sagara Y, Hara AK, Pavlicek W, Silva AC, Paden RG, Wu Q. 2010. Abdominal CT: comparison of low-dose CT with adaptive statistical iterative reconstruction and routine-dose CT with filtered back projection in 53 patients. *Am. J. Roentgenol.* 195:713–19
42. Prakash P, Kalra MK, Ackman JB, Digumarthy SR, Hsieh J, et al. 2010. Diffuse lung disease: CT of the chest with adaptive statistical iterative reconstruction technique. *Radiology* 256:261–69
43. Schulz B, Beeres M, Bodelle B, Bauer R, Al-Butmeh F, et al. 2013. Performance of iterative image reconstruction in CT of the paranasal sinuses: a phantom study. *AJNR Am. J. Neuroradiol.* 34:1072–76
44. Kalra MK, Woisetschläger M, Dahlström N, Singh S, Lindblom M, et al. 2012. Radiation dose reduction with sinogram affirmed iterative reconstruction technique for abdominal computed tomography. *J. Comput. Assist. Tomogr.* 36:339–46

45. Deák Z, Grimm JM, Treitl M, Geyer LL, Linsenmaier U, et al. 2013. Filtered back projection, adaptive statistical iterative reconstruction, and a model-based iterative reconstruction in abdominal CT: an experimental clinical study. *Radiology* 266:197–206
46. Pickhardt PJ, Lubner MG, Kim DH, Tang J, Ruma JA, et al. 2012. Abdominal CT with model-based iterative reconstruction (MBIR): initial results of a prospective trial comparing ultralow-dose with standard-dose imaging. *Am. J. Roentgenol.* 199:1266–74
47. Johnson TR. 2012. Dual-energy CT: general principles. *Am. J. Roentgenol.* 199(5 Suppl.):S3–8
48. Kaza RK, Platt JF, Cohan RH, Caoili EM, Al-Hawary MM, Wasnik A. 2012. Dual-energy CT with single- and dual-source scanners: current applications in evaluating the genitourinary tract. *Radiographics* 32:353–69
49. Karçaaltıncaba M, Aktaş A. 2011. Dual-energy CT revisited with multidetector CT: review of principles and clinical applications. *Diagn. Interv. Radiol.* 17:181–94
50. Gupta R, Phan CM, Leidecker C, Brady TJ, Hirsch JA, et al. 2010. Evaluation of dual-energy CT for differentiating intracerebral hemorrhage from iodinated contrast material staining. *Radiology* 257:205–11
51. Phan CM, Yoo AJ, Hirsch JA, Nogueira RG, Gupta R. 2012. Differentiation of hemorrhage from iodinated contrast in different intracranial compartments using dual-energy head CT. *AJNR Am. J. Neuroradiol.* 33:1088–94
52. Kemmling A, Nölte I, Groden C, Diehl S. 2011. Dual energy bone subtraction in computed tomography angiography of extracranial-intracranial bypass: feasibility and limitations. *Eur. Radiol.* 21:750–56
53. Deng K, Liu C, Ma R, Sun C, Wang XM, et al. 2009. Clinical evaluation of dual-energy bone removal in CT angiography of the head and neck: comparison with conventional bone-subtraction CT angiography. *Clin. Radiol.* 64:534–41
54. Watanabe Y, Uotani K, Nakazawa T, Higashi M, Yamada N, et al. 2009. Dual-energy direct bone removal CT angiography for evaluation of intracranial aneurysm or stenosis: comparison with conventional digital subtraction angiography. *Eur. Radiol.* 19:1019–24
55. Ferda J, Novák M, Mírka H, Baxa J, Ferdová E, et al. 2009. The assessment of intracranial bleeding with virtual unenhanced imaging by means of dual-energy CT angiography. *Eur. Radiol.* 19:2518–22
56. Miracle AC, Mukherji SK. 2009. Conebeam CT of the head and neck, part 1: physical principles. *AJNR Am. J. Neuroradiol.* 30:1088–95
57. Alspaugh J, Christodoulou E, Goodsitt M, Stayman J. 2007. Dose and image quality of flat-panel detector volume computed tomography for sinus imaging. *Med. Phys.* 34:2634
58. Gupta R, Cheung AC, Bartling SH, Lisauskas J, Grasruck M, et al. 2008. Flat-panel volume CT: fundamental principles, technology, and applications. *Radiographics* 28:2009–22
59. O'Connell A, Conover DL, Zhang Y, Seifert P, Logan-Young W, et al. 2010. Cone-beam CT for breast imaging: radiation dose, breast coverage, and image quality. *Am. J. Roentgenol.* 195:496–509
60. Cakli H, Cingi C, Ay Y, Oghan F, Ozer T, Kaya E. 2012. Use of cone beam computed tomography in otolaryngologic treatments. *Eur. Arch. Otorhinolaryngol.* 269:711–20
61. Xu J, Reh DD, Carey JP, Mahesh M, Siewerdsen JH. 2012. Technical assessment of a cone-beam CT scanner for otolaryngology imaging: image quality, dose, and technique protocols. *Med. Phys.* 39:4932–42
62. Miracle AC, Mukherji SK. 2009. Conebeam CT of the head and neck, part 2: clinical applications. *AJNR Am. J. Neuroradiol.* 30:1285–92
63. Reichardt B, Sarwar A, Bartling SH, Cheung A, Grasruck M, et al. 2008. Musculoskeletal applications of flat-panel volume CT. *Skeletal Radiol.* 37:1069–76
64. Zbijewski W, De Jean P, Prakash P, Ding Y, Stayman JW, et al. 2011. A dedicated cone-beam CT system for musculoskeletal extremities imaging: design, optimization, and initial performance characterization. *Med. Phys.* 38:4700–13
65. Zhu S, Tian J, Yan G, Qin C, Feng J. 2009. Cone beam micro-CT system for small animal imaging and performance evaluation. *Int. J. Biomed. Imaging* 2009:960573
66. Erovic BM, Chan HH, Daly MJ, Pothier DD, Yu E, et al. 2014. Intraoperative cone-beam computed tomography and multi-slice computed tomography in temporal bone imaging for surgical treatment. *Otolaryngol. Head Neck Surg.* 150:107–14
67. Zbijewski W, Beekman FJ. 2006. Efficient Monte Carlo based scatter artifact reduction in cone-beam micro-CT. *IEEE Trans. Med. Imaging* 25(7):817–27

68. Siewerdsen JH, Daly MJ, Bakhtiar B, Moseley DJ, Richard S, et al. 2006. A simple, direct method for X-ray scatter estimation and correction in digital radiography and cone-beam CT. *Med. Phys.* 33:187–97
69. Peace K, Wilensky EM, Frangos S, MacMurtrie E, Shields E, et al. 2010. The use of a portable head CT scanner in the intensive care unit. *J. Neurosci. Nurs.* 42:109–16
70. Rumboldt Z, Huda W, All JW. 2009. Review of portable CT with assessment of a dedicated head CT scanner. *AJNR Am. J. Neuroradiol.* 30:1630–36
71. Jackman AH, Palmer JN, Chiu AG, Kennedy DW. 2008. Use of intraoperative CT scanning in endoscopic sinus surgery: a preliminary report. *Am. J. Rhinol.* 22(2):170–74
72. Ginat DT, Swearingen B, Curry W, Cahill D, Madsen J, Schaefer PW. 2014. 3 Tesla intraoperative MRI for brain tumor surgery. *J. Magn. Reson. Imaging* 39:1357–65
73. Carlson AP, Yonas H. 2012. Portable head computed tomography scanner—technology and applications: experience with 3421 scans. *J. Neuroimaging* 22(4):408–15
74. Carlson AP, Phelps J, Yonas H. 2011. Alterations in surgical plan based on intraoperative portable head computed tomography imaging. *J. Neuroimaging* 22:324–28
75. Butler WE, Piaggio CM, Constantinou C, Niklason L, Gonzalez RG, et al. 1998. A mobile computed tomographic scanner with intraoperative and intensive care unit applications. *Neurosurgery* 42:1304–11
76. LaRovere KL, Brett MS, Tasker RC, Strauss KJ, Burns JP. 2012. Head computed tomography scanning during pediatric neurocritical care: diagnostic yield and the utility of portable studies. *Neurocrit. Care* 16:251–57
77. Orchard J, Yeow JT. 2008. Toward a flexible and portable CT scanner. *Med. Image Comput. Comput. Assist. Interv.* 11(Pt. 2):188–95
78. Somenkov V, Tkalic A, Shil'shtein S. 1991. Refraction contrast in X-ray introscopy. *Sov. Phys. Tech. Phys.* 36:1309–311
79. Momose A, Takeda T, Itai Y, Hirano K. 1996. Phase-contrast X-ray computed tomography for observing biological soft tissues. *Nat. Med.* 2:473–75
80. Chapman D, Thomlinson W, Johnston RE, Washburn D, Pisano E, et al. 1997. Diffraction enhanced X-ray imaging. *Phys. Med. Biol.* 42:2015–25
81. Tapfer A, Bech M, Velroyen A, Meiser J, Mohr J, et al. 2012. Experimental results from a preclinical X-ray phase-contrast CT scanner. *Proc. Natl. Acad. Sci. USA* 109:15691–96
82. Zhou SA, Brahme A. 2008. Development of phase-contrast X-ray imaging techniques and potential medical applications. *Phys. Med.* 24(3):129–48
83. Tapfer A, Bech M, Pauwels B, Liu X, Bruyndonckx P, et al. 2011. Development of a prototype gantry system for preclinical X-ray phase-contrast computed tomography. *Med. Phys.* 38(11):5910–15
84. Hemberg O, Otendal M, Hertz HM. 2003. Liquid-metal-jet anode electron-impact X-ray source. *Appl. Phys. Lett.* 83:1483e5